Tuning Magnetization Dynamics with Strong Spin-Orbit Coupling in Transition-Metal Dichalcogenide/Co-Fe-B Heterostructures

Guanjie Wu,[1] Yang Ren,[2] Xiaodong He,[2] Yu Zhang,[1] Hongwei Xue,[1] Zhihao Ji,[1] Q. Y. Jin,[1] and Zongzhi Zhang[1,*]

[1] *Shanghai Engineering Research Center of Ultra-Precision Optical Manufacturing and Key Laboratory of Micro and Nano Photonic Structures (MOE), Department of Optical Science and Engineering, Fudan University, Shanghai 200433, China*

[2] *School of Physics and Astronomy, Yunnan University, Kunming 650091, China*

(Received 18 September 2019; revised manuscript received 3 December 2019; accepted 27 January 2020; published 12 February 2020)

Spintronic materials with two-dimensional (2D) transition-metal dichalcogenide (TMD)/ferromagnet (FM) interfaces have received a great deal of interest recently due to strong modulation of the magnetic properties, which provide attractive opportunities for magnetic information storage. Here, we demonstrate the strong spin-orbit coupling (SOC) effect and great interfacial tuning of magnetization dynamics in MX_2/Co-Fe-B thin films by means of a time-resolved magneto-optical Kerr approach, where M is chosen as Mo or W and X is S or Se. The significant drop of demagnetization time, τ_m, and increase of magnetic damping factor, α_s, clearly highlight the presence of high interfacial SOC strength in just one monolayer of MoS_2. Compared with the single Co-Fe-B film, the precession frequency, f, is lowered after inserting a MX_2 layer, suggesting a reduction of the effective magnetization, $4\pi M_{\text{eff}}$, originating from the interfacial d-d hybridization effect. The role of SOC strength on τ_m, M_{eff}, and α_s is confirmed by using different TMD materials, and thus, demonstrates that the element M plays a dominant role. The samples with WS_2 or WSe_2 have much shorter τ_m, smaller M_{eff}, and larger α_s values due to the strong SOC interaction of heavier atoms. The observed efficient control of dynamic magnetic behavior will further promote the development of TMD/FM materials for practical spintronic applications with ultrafast manipulation speed and low energy consumption.

DOI: 10.1103/PhysRevApplied.13.024027

I. INTRODUCTION

The efficient generation of spin current in low-dimensional magnetic systems has promoted numerous investigations and found practical applications in energy-efficient spintronic devices, including spin-transfer torque and spin-orbit torque (SOT) magnetic random access memories, nano-oscillators, logic devices, and sensors [1–8]. Pure spin current can be generated by various methods, such as spin pumping and spin Hall effects [9,10], in which spin pumping is a widely accepted method of spin injection into an adjacent heavy-metal (HM) layer. Most research in the last decade has focused on magnetic thin films in contact with a conventional HM layer, e.g., Pt, Pd, Ta, and W with a thickness of several nanometers. In terms of their high spin-orbit interaction (SOI) strength, strong current-driven SOT torques can be produced, which act on the magnetic layer to drive magnetization reversal or maintain persistent oscillation [11–13]. Compared with these HM films, two-dimensional (2D) materials, such as graphene and transition-metal dichalcogenide (TMD), have attracted a great deal of interest recently because of their distinctive electronic, optical, and catalytic properties [14–17]. Graphene has been extensively investigated due to the possibility of a long spin lifetime arising from weak intrinsic SOC [7,18,19]. In contrast, TMD materials have a much stronger SOC and are considered as promising candidates for spintronic applications [20–27]. The strong SOC interaction will inevitably affect the magnetic properties of the adjacent ferromagnetic (FM) layer. For instance, a large SOT generated by current-induced spin accumulation has been reported in TMD/Co-Fe-B bilayers [20]. Nevertheless, so far, relevant studies are largely related to spin-torque ferromagnetic resonance or electrical transport measurement methods [5,17,22]; the influence of TMD materials on the transient magnetization behavior in the time domain have not yet been clearly clarified. From the potential application perspective, it is essential to perform a detailed study on the magnetic dynamic behavior of the TMD/FM system because it is of significant importance in achieving ultrafast control of magnetization orientation and reducing power consumption.

*zzzhang@fudan.edu.cn

The all-optical pump-and-probe technique based on the time-resolved magneto-optical Kerr effect (TR MOKE) is an excellent approach for the excitation and detection of magnetization dynamics [28], which allows us to gain a deep insight into the roles of adjacent TMD materials. Usually, the laser-induced magnetization dynamic behavior consists of an ultrafast demagnetization process taking place within a subpicosecond range and a subsequent magnetization precession process lasting for tens to hundreds of picoseconds [29,30]. It is now widely believed that the SOI strength determines the angular momentum transfer rate of a spin system [31–33], which plays an important role in the demagnetization process and provides a great way to speed up the process. Moreover, the spin-pumping efficiency is also associated with the interface between FM and nonmagnetic (NM) layers [34–36]. The strong SOC interaction of the TMD material at the FM/NM interface could facilitate propagation and dissipation of the transverse spin current generated by magnetization precession, which may affect the precession behavior and give rise to a large spin-pumping contribution to the magnetic damping factor because of the stronger interaction between electron spin and lattice. As a result, to gain a comprehensive view of the features of magnetization dynamics in the TMD/Co-Fe-B system, here, we perform a systematic study on a heterostructure of MX_2/Co-Fe-B($t_{\text{Co-Fe-B}}$), where M is Mo or W and X is S or Se. By varying the layer number and element type of MX_2, the SOC strength is well adjusted. From the temporal magnetization dynamics spectra measured by means of TR MOKE, the dynamic magnetic properties, including the ultrafast demagnetization time, magnetization precession frequency, and magnetic damping factor, are determined and their dependencies on MX_2 are well clarified. The findings in this work enable us to obtain a deep understanding of the magnetization dynamics and might shed light on further developments in the attractive TMD-based system.

II. EXPERIMENTAL METHOD

High-quality TMD films of MX_2 (M = Mo, W; X = S, Se) are grown on thermally oxidized silicon substrates with a 300-nm thick SiO_2 layer by using the chemical vapor deposition method. During the fabrication process, the transition-metal trioxides of MoO_3 and WO_3 are vaporized and reacted with S or Se vapor in a chamber under a controlled temperature and gas environment. The accurate film thickness or monolayer (ML) number, n_L (considering the thickness of one monolayer to be 0.65 nm), is achieved by controlling the time of growth and is then calibrated by means of topographical atomic force microscopy (AFM). The AFM images for MoS_2 films indicate that the average roughness value is as small as 0.11–0.35 nm. Details of the fabrication process and structural characterization are given in Appendixes A and B, respectively. After the deposition of TMDs, the samples are then immediately transferred into the sputtering system for magnetic-layer deposition. Then, three series of samples with structures of Si/SiO_2/MoS_2(n_L = 3 ML)/Co-Fe-B ($t_{\text{Co-Fe-B}}$ = 2–10 nm)/Al(5 nm), Si/SiO_2/MoS_2(1–10 ML)/Co-Fe-B(3 nm)/Al(5 nm), and Si/SiO_2/MX_2(3 ML)/CFB (3 nm)/Al (5 nm) are deposited sequentially at room temperature in a Kurt J. Lesker magnetron sputtering system under a base pressure better than 3×10^{-8} Torr. The deposition rates of Co-Fe-B and Al layers are optimized as 0.45 and 0.43 Å/s, respectively. For comparison, reference samples of Si/SiO_2/Co-Fe-B($t_{\text{Co-Fe-B}}$)/Al(5 nm) are also prepared.

The static magnetic properties are measured by using a vibrating sample magnetometer (VSM), whereas the magnetization dynamics are acquired by means of the TR MOKE technique using a pulsed Ti:sapphire laser with a central wavelength of 800 nm, a pulse duration of 150 fs, and a repetition rate of 1 kHz. The dynamic behaviors are excited by an intense pump pulse beam with a fluence of about 1.0 mJ/cm^2 traveling through an optical delay line, and the transient Kerr rotation signals are detected by a time-delayed weak probe beam of about 0.05 mJ/cm^2. In our TR MOKE experiments, the spot diameters of the pump and probe laser pulses are 2.0 and 0.2 mm, respectively. Moreover, the probe beam spot is always located in the center of the pump spot, so that no inhomogeneous precessional motion can be generated [37]. The transient Kerr signals are read out by a lock-in amplifier with an optical chopper, which modulates the pump beam at a frequency of 108 Hz. To avoid the impact of magnetization precession on the ultrafast demagnetization process, the temporal Kerr signal is detected in two different field configurations. For the demagnetization process measurement, the respective incident angles of pump and probe beam are 5° and 45°, respectively, with respect to the sample normal. The magnetic field, H, is parallel to the sample plane to restrict magnetization along its easy-axis direction. In contrast, for magnetization precession behaviors, both the pump and probe beam are at an almost perpendicular incidence. Moreover, the applied H is at a tilted angle of 19° with respect to the film plane to drive the magnetization away from its easy plane.

III. RESULTS AND DISCUSSION

A. Magnetic measurements of MoS_2 (n_L)/Co-Fe-B($t_{\text{Co-Fe-B}}$)

Figure 1(a) shows the schematic diagram of the film layer structure and experimental geometry for TR MOKE measurements. The pump and probe beams are spatially overlapped on the sample surface to locally excite and probe the magnetization dynamics. Figure 1(b) shows the typical laser-induced demagnetization process for the 3-nm thick Co-Fe-B sample measured under a saturation

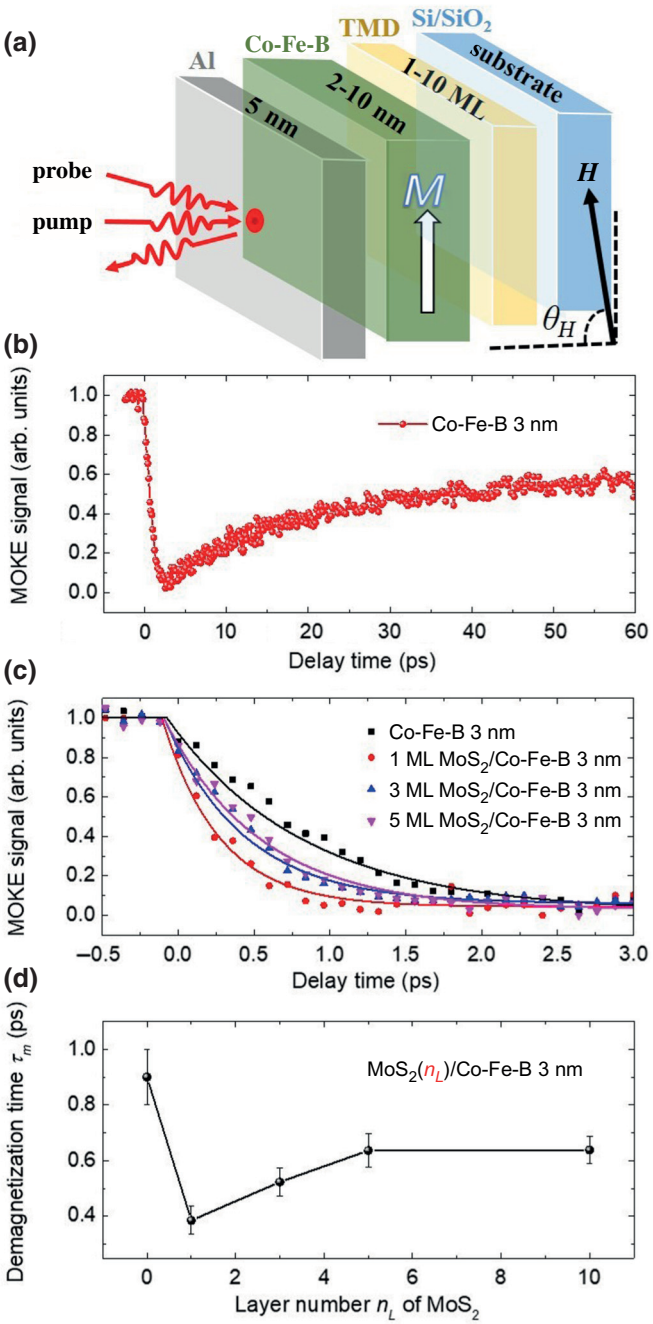

FIG. 1. (a) Illustration of the sample layer structure and experimental geometry for TR MOKE measurements. (b) Typical laser-induced demagnetization and magnetization relaxation curves for the single Co-Fe-B(3 nm) film under $H = 6.0$ kOe. (c) Short-range demagnetization curves of $MoS_2(n_L = 0, 1, 3,$ and 5 ML)/Co-Fe-B(3 nm) samples. (d) Fitted demagnetization time, τ_m, as a function of n_L for samples of $MoS_2(n_L)$/Co-Fe-B(3 nm).

in-plane field of $H = 6.0$ kOe. The transient MOKE signals decrease immediately upon laser excitation, which takes place within a subpicosecond range and is followed by a slow recovery process. Figure 1(c) shows only the ultrafast demagnetization process of $MoS_2(n_L = 0, 1, 3,$ and 5 ML)/Co-Fe-B(3 nm) samples at the short-range delay time of $t = 0$–3 ps, from which the ultrafast demagnetization time (τ_m) can be fitted with an exponential decay expression [38]

$$\theta(t) = \theta(0) + A\exp[-(t-c)/\tau_m], \quad (1)$$

where $\theta(0)$ is the Kerr signal at $t = 0$. A and τ_m are the amplitude and lifetime of the demagnetization process, respectively. The fitted τ_m values are displayed in Fig. 1(d) as a function of n_L. For the single Co-Fe-B sample without a MoS_2 underlayer ($n_L = 0$), τ_m is around 0.9 ps, which decreases significantly down to 0.4 ps for $n_L = 1$, clearly highlighting the presence of a strong interfacial SOC in only 1-ML thick MoS_2. Nevertheless, with an increase in n_L, τ_m rises gradually and becomes saturated at $n_L \geq 5$, which is likely to be due to weakening of the 2D characteristics, corresponding to a reduced strength of the interfacial SOC [21].

Below, we analyze the long-range precession dynamics measured under a tilted magnetic field of $\theta_H = 71°$. Figure 2(a) shows the TR MOKE spectra for the MoS_2(3 ML)/Co-Fe-B($t_{\text{Co-Fe-B}} = 2$, 5, and 10 nm) samples measured at $H = 15$ kOe, together with those of the single Co-Fe-B($t_{\text{Co-Fe-B}}$) films for comparison. By fitting these dynamic Kerr signals with an exponentially damped sine function of

$$\theta_k = a + b\exp(t/t_0) + c\sin(2\pi ft + \varphi)\exp(-t/\tau), \quad (2)$$

the precession frequency, f, and decay time, τ, in the third term can be derived. The fitted frequency values are shown in Fig. 2(b) as a function of H. First, we can see that at a fixed H, the f value increases with the increase of $t_{\text{Co-Fe-B}}$. Second, after inserting a 3-ML thick MoS_2 underlayer, the field-dependent frequency curves are shifted downwards, especially for the sample with a thick Co-Fe-B layer. To clarify the observed variation trends, the frequency curves are fitted by using the following Kittle formula of uniform precession mode [39]:

$$2\pi f = \gamma\sqrt{H_1 H_2}, \quad (3)$$

where $H_1 = H\cos(\theta - \theta_H) - 4\pi M_{\text{eff}}\cos 2\theta$ and $H_2 = H\cos(\theta - \theta_H) - 4\pi M_{\text{eff}}\cos^2\theta$. $\gamma = \gamma_e g/2$ is the gyromagnetic ratio, with $\gamma_e = 1.76 \times 10^7$ Hz/Oe; g is the Lande splitting factor and is taken to be 2.1 for Co-Fe-B [40]. The magnetization equilibrium angle, θ, can be determined from $2H\sin(\theta - \theta_H) = 4\pi M_{\text{eff}}\sin 2\theta$. As shown in Fig. 2(c), after introducing a 3 ML MoS_2 layer, the fitted effective magnetization, $4\pi M_{\text{eff}}$ (solid symbols), is obviously reduced. Nevertheless, the two sample series both display a linear decreasing trend with the increase of $1/t_{\text{Co-Fe-B}}$. The observed variation trend of $4\pi M_{\text{eff}}$ and the effect of MoS_2 are confirmed by VSM measurements.

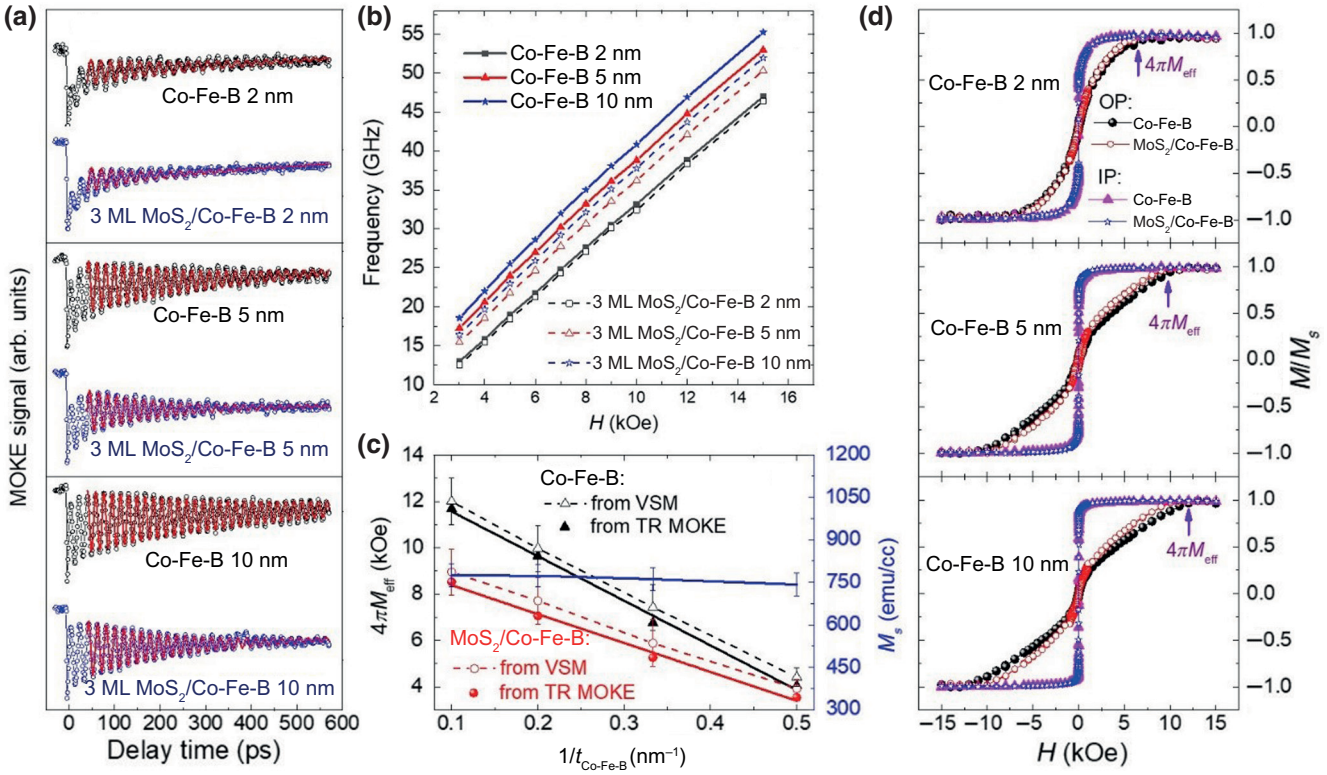

FIG. 2. (a) Dynamic TR MOKE signals measured under $H = 15$ kOe for the single Co-Fe-B($t_{\text{Co-Fe-B}}$) and 3 ML MoS_2/Co-Fe-B($t_{\text{Co-Fe-B}}$) samples, where $t_{\text{Co-Fe-B}}$ is 2, 5, and 10 nm. (b) Corresponding precession frequency as a function of H. (c) The $1/t_{\text{Co-Fe-B}}$ dependences of effective magnetization, $4\pi M_{\text{eff}}$, obtained from both the TR MOKE and VSM measurements. Saturation magnetization, M_s, of MoS_2(3 ML)/Co-Fe-B($t_{\text{Co-Fe-B}}$) samples measured by VSM are also shown. (d) Out-of-plane (OP) and in-plane (IP) magnetic hysteresis loops for these samples.

Figure 2(d) shows the corresponding OP and IP magnetization hysteresis loops. The magnetic field at the intersection point of the OP and IP loops is generally defined as the effective magnetization, as indicated by the arrows. Indeed, the $4\pi M_{\text{eff}}$ value increases with increasing $t_{\text{Co-Fe-B}}$ and is apparently smaller for the MoS_2/Co-Fe-B samples. The $4\pi M_{\text{eff}}$ values obtained from VSM are also presented in Fig. 2(c); these values are in good accordance with the curves obtained by means of TR MOKE. Relative to the linear reduction of M_{eff} with $1/t_{\text{Co-Fe-B}}$, the saturation magnetization, M_s, of MoS_2(3 ML)/Co-Fe-B($t_{\text{Co-Fe-B}}$) samples measured by VSM remains nearly unchanged, as shown in Fig. 2(c), which indicates that the decreasing trend of M_{eff} mainly comes from the contribution of interfacial perpendicular anisotropy.

Then, the curves of $4\pi M_{\text{eff}}$ versus $1/t_{\text{Co-Fe-B}}$ obtained through the TR MOKE technique are fitted to

$$4\pi M_{\text{eff}} = 4\pi M_s - \frac{2K_s}{M_s t_{\text{Co-Fe-B}}}, \tag{4}$$

through which the surface anisotropy constant, K_s, and the saturation magnetization, M_s, can be determined. The values of M_s and K_s of the single Co-Fe-B film are deduced to be 1073 emu/cc and 1.03 erg/cm^2, respectively, which decrease to 766 emu/cc and 0.48 erg/cm^2, respectively, for the Co-Fe-B layer deposited on top of 3 ML MoS_2. This phenomenon can be attributed to the hybridization effect of Mo 4*d* electrons coupled with Co/Fe 3*d* electrons at the interface, which may enhance the SOC strength [3]. As revealed from density functional theory calculations, this hybridization induces a magnetic moment in the adjacent Mo atoms aligned antiparallel to the Co and Fe moments, and consequently, gives rise to the reduction in M_s [41].

Figure 3(a) shows the field-dependent frequency curves for the $MoS_2(n_L)$/Co-Fe-B(3 nm) samples with various n_L. Similarly, by fitting these curves with Eq. (3), the $4\pi M_{\text{eff}}$ values are obtained and shown in Fig. 3(b). Interesting, with increasing n_L, $4\pi M_{\text{eff}}$ shows very similar behavior to that of τ_m. It also decreases dramatically at $n_L = 1$ and then increases gradually. This nonmonotonic variation trend is also confirmed by the VSM results, as displayed in Fig. 3(b). The initial large decrease at $n_L = 1$ should arise from the hybridization effect introduced previously, whereas the subsequent increase with n_L can be attributed to the increased bulk property of MoS_2, which weakens the interfacial hybridization effect.

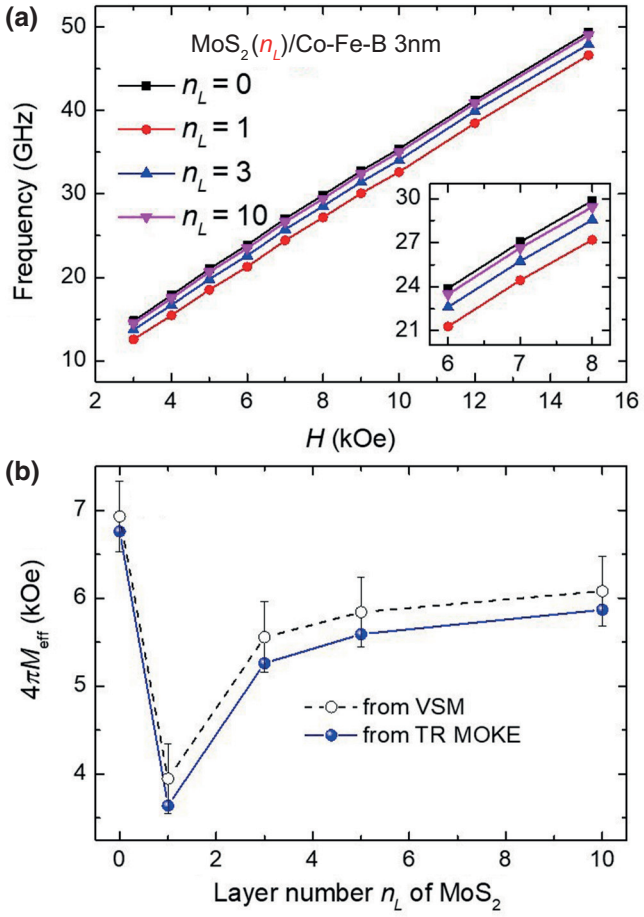

FIG. 3. (a) Precession frequency as a function of H for samples of $MoS_2(n_L)$/Co-Fe-B(3 nm) with various n_L. The inset clearly shows the frequency shift in the range of 6–8 kOe. (b) Effective magnetization, $4\pi M_{\text{eff}}$, versus n_L obtained from TR MOKE and VSM results.

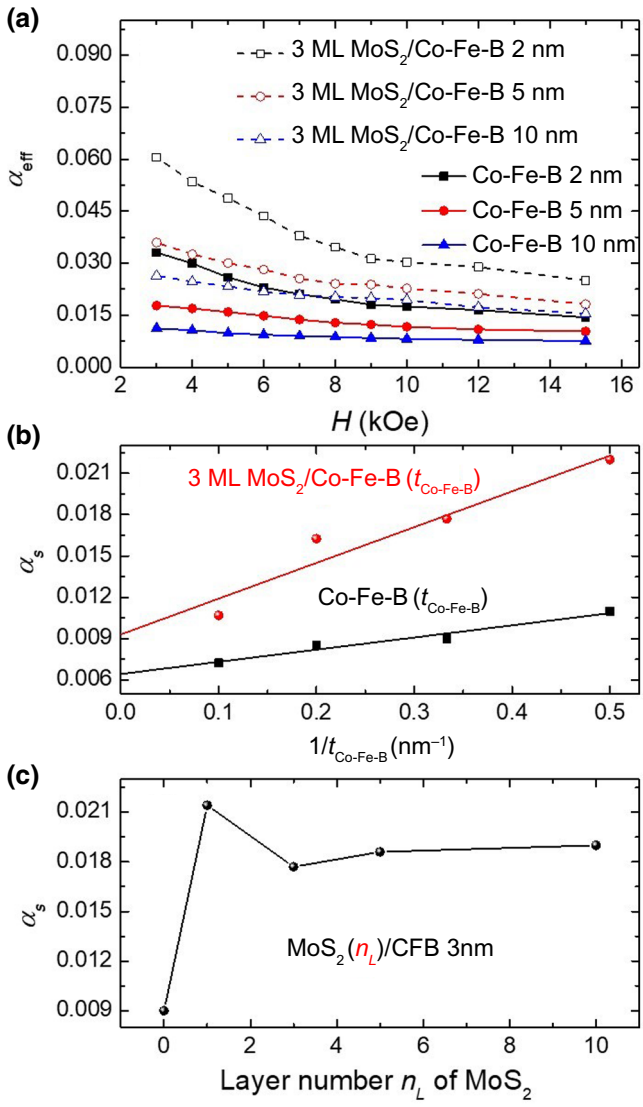

FIG. 4. (a) Dependence of effective magnetic damping factor, α_{eff}, on the magnetic field, H, for samples of single Co-Fe-B($t_{\text{Co-Fe-B}}$) and $MoS_2(n_L)$/Co-Fe-B($t_{\text{Co-Fe-B}}$). (b) Saturated damping factor, α_s, as a function of $1/t_{\text{Co-Fe-B}}$. (c) Variation of α_s with monolayer number, n_L, of MoS_2.

According to the simple approximate equation of $\alpha_{\text{eff}} = 1/(2\pi f\tau)$, the effective magnetic damping factor, α_{eff}, is calculated and shown in Fig. 4(a), which includes both the intrinsic damping and extrinsic contributions that arise from spin pumping and magnetic inhomogeneities [42, 43]. With the increase of H, α_{eff} gradually decreases and reaches a nearly saturated value because extrinsic damping related to inhomogeneous magnetic distributions is largely eliminated. To accurately illustrate the influence of the TMD underlayer on magnetic damping, the curves in Fig. 4(a) are fitted using a decaying exponential function of $\alpha_{\text{eff}} = \alpha_s + \alpha_{\text{ex0}}\exp(-H/H_0)$, where α_s corresponds to the damping value at an infinite H [40]. Figure 4(b) shows the fitted α_s as a function of the inverse of $t_{\text{Co-Fe-B}}$. Notably, at each Co-Fe-B thickness, the α_s value of 3 ML MoS_2/Co-Fe-B ($t_{\text{Co-Fe-B}}$) is larger than the single Co-Fe-B film. Moreover, no matter if the Co-Fe-B film is with or without MoS_2, α_s rises nearly linearly with the increase of $1/t_{\text{Co-Fe-B}}$. It is believed that the spin-pumping effect, i.e., the spin-current dissipation inside the nonmagnetic MoS_2 layer, is responsible for the enhanced magnetic damping [44]. According to the spin-pumping-effect theory, the correlation between α_s and $t_{\text{Co-Fe-B}}$ can be expressed as [45]

$$\alpha_s = \alpha_0 + \frac{g\mu_B g_{\text{eff}}^{\uparrow\downarrow}}{4\pi M_s}\frac{1}{t_{\text{Co-Fe-B}}}, \tag{5}$$

where the intrinsic Gilbert damping, α_0, and interfacial spin-mixing conductance, $g_{\text{eff}}^{\uparrow\downarrow}$, can be extracted from the intercept and slope of the straight lines shown in Fig. 4(b). The obtained α_0 value for 3 ML MoS_2/Co-Fe-B is 0.009, which is slightly higher than the value of 0.006 for the single Co-Fe-B film. Such a difference may come from a small change in the SOC strength or in the density of state at the

Fermi level induced by the MoS_2 underlayer [46,47]. In contrast, due to the strong SOC effect of MoS_2, the derived $g_{\text{eff}}^{\uparrow\downarrow}$ value is quite different. It is 16.11×10^{19} m^{-2} for 3 ML MoS_2/Co-Fe-B, which is three times larger than that of the single Co-Fe-B film. To fully understand the role of MoS_2 on the magnetic damping factor, α_s as a function of monolayer number, n_L, is shown in Fig. 4(c). Compared with the value of 0.009 for the Co-Fe-B(3 nm) layer, the saturated damping factor is seen to increase significantly up to 0.021 at $n_L = 1$ and then drops at $n_L = 3$ for the sample of $MoS_2(n_L)$/Co-Fe-B(3 nm). The variation tendency is opposite to those of the demagnetization time, τ_m, in Fig. 1(d) and the effective magnetization, $4\pi M_{\text{eff}}$, in Fig. 3(b), which can be interpreted by competition between the interfacial SOC strength and the increased bulk property. It is important to note that, when n_L exceeds three, we observe a slight increase in α_s, which is typically observed in the HM/FM bilayers due to the reduced backflow spin current caused by spin diffusion in the thick HM layer [48,49].

B. Magnetic measurements of 3 ML MX_2/Co-Fe-B(3 nm)

To further confirm the SOC role of the TMD underlayer, another series of samples with a structure of 3 ML MX_2/Co-Fe-B(3 nm) with different MX_2 materials are prepared, where MX_2 is MoS_2, $MoSe_2$, WS_2, and WSe_2. Figure 5(a) shows the demagnetization curves for these samples. Obviously, due to the enhanced interfacial SOC strength by *d-d* hybridization, τ_m of all MX_2/Co-Fe-B samples is shorter than that of the single Co-Fe-B film. Moreover, compared with element of X in MX_2, it is found that M plays a more significant role on τ_m. The demagnetization time for the case of WS_2 or WSe_2 is apparently faster than that of MoS_2 or $MoSe_2$, which results from the stronger SOC interaction for heavier atoms [6,20,21]. In addition, the impact of TMD material on the dynamic precession process is also investigated. The precession frequency values are shown in Fig. 5(b), from which $4\pi M_{\text{eff}}$ is fitted to be 5.20, 5.47, 4.43, and 3.19 kOe for $MX_2 = MoS_2$, $MoSe_2$, WS_2, and WSe_2, respectively; all of these values are lower than that of 6.76 kOe for the single Co-Fe-B film. Apparently, due to the relatively stronger surface hybridization of heavier metal W 5*d* electrons coupled with Co/Fe 3*d* electrons, the WX_2 underlayer generates a greater reduction in the effective magnetization than that of MoX_2, which shares the same trend as that of τ_m. The corresponding effective magnetic damping factor, α_{eff}, is also calculated and shown in Fig. 5(c). As expected, the saturated damping, α_s, of Co-Fe-B (3 nm) increases clearly after inserting a MX_2 underlayer due to the spin-pumping effect. Moreover, the influence of element M in MX_2 is much stronger than that of element X. One can see, relative to samples with a MoX_2 underlayer, a much larger α_s of 0.030 is obtained for the case of the WX_2 underlayer, which should be attributed again to the higher SOC strength of heavier W atoms.

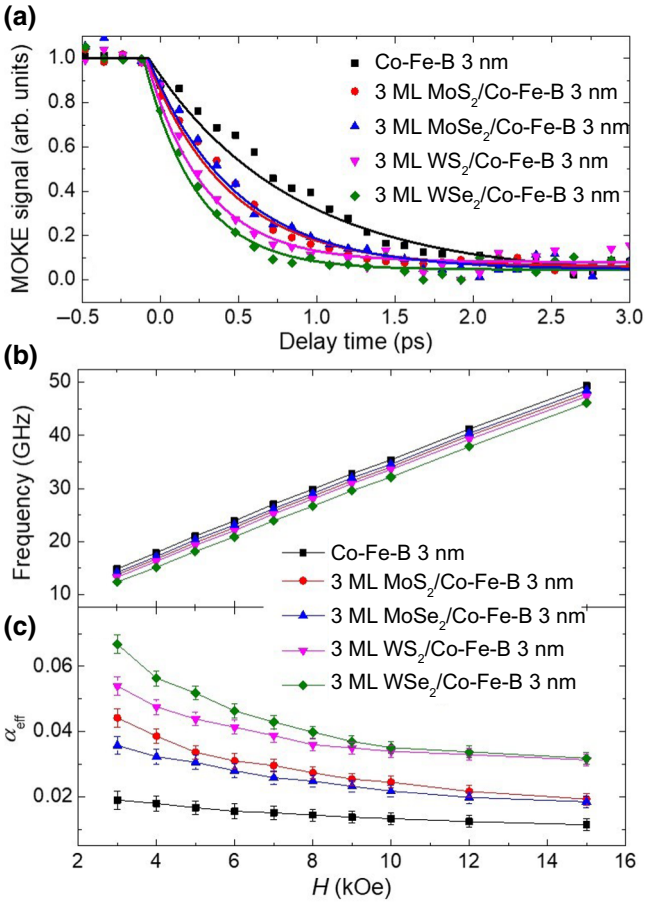

FIG. 5. (a) Demagnetization curves for Co-Fe-B(3 nm) film with or without a 3 ML MX_2 underlayer. Corresponding field-dependent frequency curves (b) and effective magnetic damping factor α_{eff} (c).

IV. SUMMARY

The magnetization dynamics in $MoS_2(n_L)$/Co-Fe-B ($t_{\text{Co-Fe-B}}$) and 3 ML MX_2/Co-Fe-B(3 nm) bilayers are systematically investigated by means of the TR MOKE technique. By varying the monolayer number of MoS_2 and the material type of MX_2, the SOC strength can be readily adjusted, which leads to dramatic modulations of the static and dynamic magnetic properties, including the effective magnetization, $4\pi M_{\text{eff}}$; demagnetization time, τ_m; precession frequency, f; and saturated magnetic damping factor, α_s. Due to the *d-d* hybridization effect between MoS_2 and Co-Fe-B, the $4\pi M_{\text{eff}}$ values are reduced, which gives rise to the observed changes in f. Meanwhile, with an increase in n_L, a similar nonmonotonic variation trend is found for τ_m and $4\pi M_{\text{eff}}$, but contrary to that of α_s. The greatly decreased τ_m and enhanced α_s at $n_{\text{L}} = 1$ can be ascribed to the significant

SOC strength of MoS_2, while their subsequent gradual changes at $n_L > 1$ are related to the increased bulk effect. Furthermore, these impacts of the TMD underlayer on the magnetic properties are confirmed by varying the specific materials. Our findings suggest an alternative efficient approach for the control of dynamic magnetic properties in two-dimensional TMD/FM heterostructures, which is of great significance for the development of ultrafast data storage and microwave devices.

ACKNOWLEDGMENTS

This work is supported by the National Natural Science Foundation of China (Grants No. 11874120, No. 51671057, and No. 11474067).

APPENDIX A

Here, we provide fabrication details of MoS_2, $MoSe_2$, WS_2, and WSe_2 films by means of chemical vapor deposition.

A. Growth of MoS_2

MoO_3 (99.999% purity) and solid sulfur (99.999% purity) are used as the molybdenum and sulfur sources, respectively. Meanwhile, Ar is used as the growth carrier gas. A two-temperature-zone tube furnace with a diameter of 80 mm is used for heating, in which MoO_3 and sulfur are heated to 650 °C and 180 °C, respectively. The deposition rate is controlled by adjusting the Ar pressure and deposition time. The 1 ML film is grown under a pressure of 4 kPa for 10 min, whereas, for the thicker film, the rate is increased to 5 min/ML by reducing the growth Ar pressure.

B. Growth of $MoSe_2$

MoO_3 (99.999% purity) and solid selenium particles (99.999% purity) are used as the molybdenum and selenium sources, respectively. Meanwhile, 90% Ar and 10% H_2 are used as the growth carrier gas. MoO_3 and selenium are heated to 750 °C and 260 °C, respectively, by using a two-temperature-zone tube furnace.

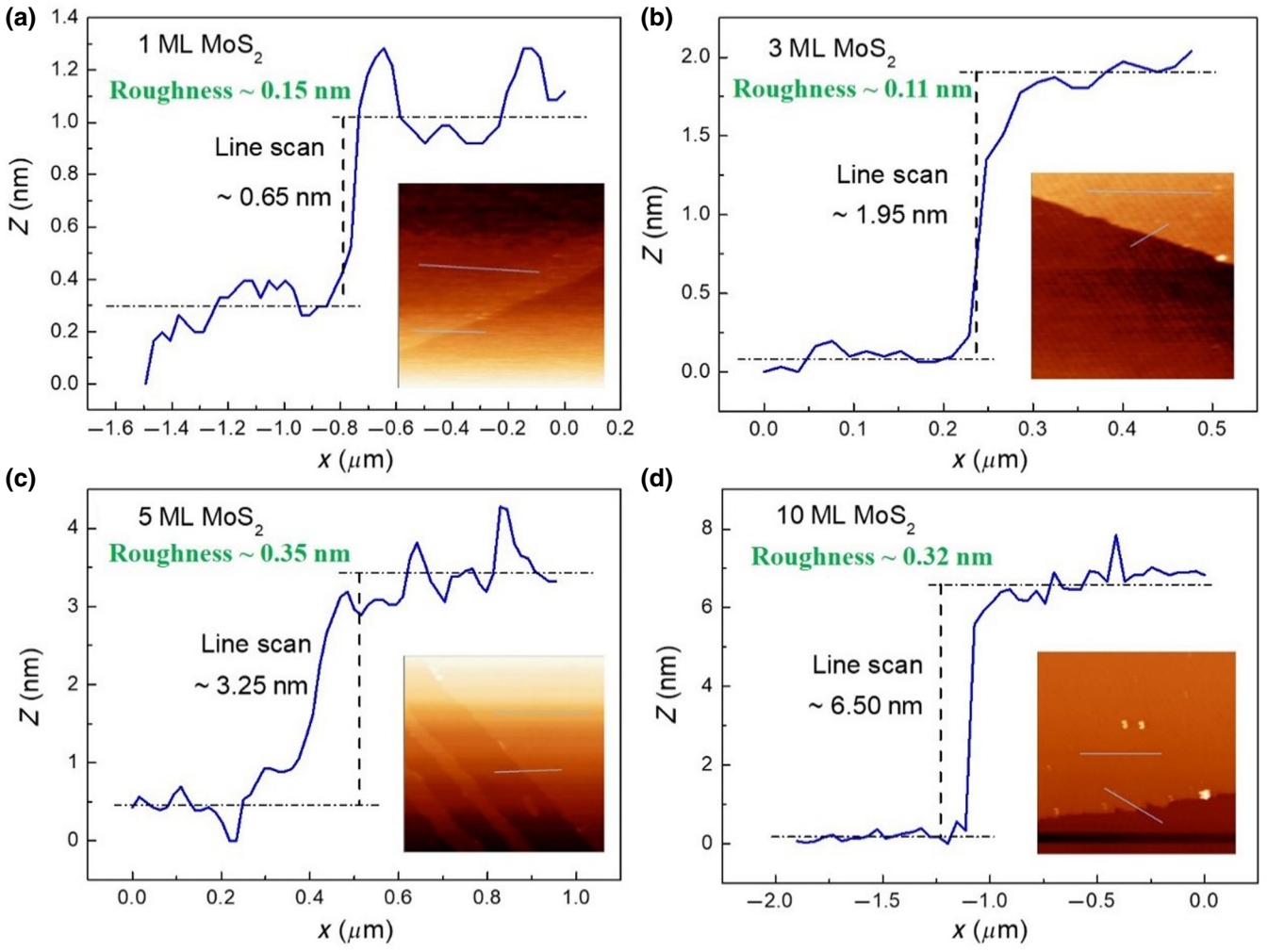

FIG. 6. Line-scan profiles recorded on the step for different thicknesses of MoS_2 layers: (a) 1, (b) 3, (c) 5, and (d) 10 ML. Insets are the corresponding AFM images.

C. Growth of WS_2

High-purity WO_3 and sulfur are used as the tungsten and sulfur sources, respectively. Meanwhile, Ar and H_2 with flows of 200 and 20 sccm, respectively, are used as the growth carrier gas. A three-temperature-zone tube furnace is used for heating, in which WO_3 and sulfur are heated to 1000 °C and 200 °C, respectively.

D. Growth of WSe_2

High-purity WO_3 and solid selenium particles are used as the tungsten and selenium sources, respectively. Meanwhile, Ar and H_2 with flows of 100 and 10 sccm, respectively, are used as the growth carrier gas. A two-temperature-zone tube furnace is used for heating, in which WO_3 is placed in the high-temperature area to be heated to 990 °C, and selenium is placed in the low-temperature area to be heated to 250 °C.

APPENDIX B

We characterize the MoS_2 film thickness and corresponding surface roughness by means of topographical AFM. As shown in Fig. 6, the average roughness value is rather small, around 0.15, 0.11, 0.35, and 0.32 nm for 1, 3, 5, and 10 ML MoS_2, respectively, showing the high quality of the TMDs. Additionally, the line-scan profile recorded over the height step shown in Fig. 6 confirms that the thickness of the MoS_2 films is 1, 3, 5, and 10 ML.

Figure 7 shows the Raman spectra of different MoS_2 films. For the 1 ML sample, the spectrum exhibits two characteristic bands: the in-plane phonon mode, E^1_{2g}, centered near 385^{-1} cm^{-1}, and the out-of-plane phonon mode, A_{1g}, centered near 405 cm^{-1}, with a peak frequency difference of 20 cm^{-1}, which is a clear signature of monolayer MoS_2. One can see that the positions of the E^1_{2g} and A_{1g} modes change with increasing monolayer number; the variation trend of separations between the two modes are consistent with the results reported by Shao *et al*. [20].

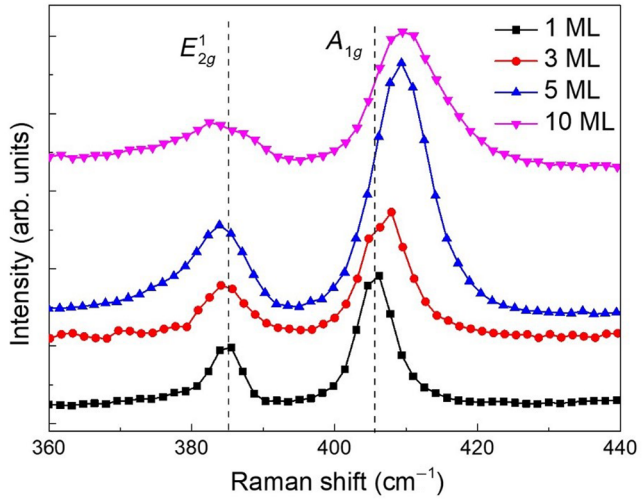

FIG. 7. Raman spectra of the MoS_2 films with different thicknesses.

[1] A. Ramasubramaniam and D. Naveh, Mn-doped monolayer MoS2: An atomically thin dilute magnetic semiconductor, Phys. Rev. B **87**, 195201 (2013).

[2] K. Dolui, A. Narayan, I. Rungger, and S. Sanvito, Efficient spin injection and giant magnetoresistance in Fe/MoS2/Fejunctions, Phys. Rev. B **90**, 041401 (2014).

[3] C. Song, S. Gong, Z. Zhang, H. Mao, Q. Zhao, J. Wang, and H. Xing, Tuning magnetic anistropy by charge injection and strain in Fe/MoS2 bilayer heterostructures, J. Phys. D: Appl. Phys. **48**, 485001 (2015).

[4] M. H. D. Guimaraes, G. M. Stiehl, D. MacNeill, N. D. Reynolds, and D. C. Ralph, Spin-Orbit torques in NbSe2/permalloy bilayers, Nano Lett. **18**, 1311 (2018).

[5] J. B. S. Mendes, A. Aparecido-Ferreira, J. Holanda, A. Azevedo, and S. M. Rezende, Efficient spin to charge current conversion in the 2D semiconductor MoS2 by spin pumping from yttrium iron garnet, Appl. Phys. Lett. **112**, 242407 (2018).

[6] W. Lv, Z. Jia, B. Wang, Y. Lu, X. Luo, B. Zhang, Z. Zeng, and Z. Liu, Electric-field control of spin-orbit torques in WS2/permalloy bilayers, ACS. Appl. Mater. Interfaces **10**, 2843 (2018).

[7] D. Pesin and A. H. MacDonald, Spintronics and pseudospintronics in graphene and topological insulators, Nat. Mater. **11**, 409 (2012).

[8] Liang Cheng, Xinbo Wang, Weifeng Yang, Jianwei Chai, Ming Yang, Mengji Chen, Yang Wu, Xiaoxuan Chen, Dongzhi Chi, Kuan Eng Johnson Goh, Jian-Xin Zhu, Handong Sun, Shijie Wang, Justin C. W. Song, Marco Battiato, Hyunsoo Yang, and Elbert E. M. Chia, Far out-of-equilibrium spin populations trigger giant spin injection into atomically thin MoS2, Nat. Phys. **15**, 347 (2019).

[9] K. Chen and S. Zhang, Spin Pumping in the Presence of Spin-Orbit Coupling, Phys. Rev. Lett. **114**, 126602 (2015).

[10] A. Soumyanarayanan, N. Reyren, A. Fert, and C. Panagopoulos, Emergent phenomena induced by spin-orbit coupling at surfaces and interfaces, Nature **539**, 509 (2016).

[11] I. M. Miron, K. Garello, G. Gaudin, P. J. Zermatten, M. V. Costache, S. Auffret, S. Bandiera, B. Rodmacq, A. Schuhl, and P. Gambardella, Perpendicular switching of a single ferromagnetic layer induced by in-plane current injection, Nature **476**, 189 (2011).

[12] L. Liu, C. F. Pai, Y. Li, H. W. Tseng, D. C. Ralph, and R. A. Buhrman, Spin-torque switching with the giant spin Hall effect of tantalum, Science **336**, 555 (2012).

[13] F. Freimuth, S. Blugel, and Y. Mokrousov, Spin-orbit torques in Co/Pt(111) and Mn/W(001) magnetic bilayers from first principles, Phys. Rev. B **90**, 174423 (2014).

[14] A. Kuc, N. Zibouche, and T. Heine, Influence of quantum confinement on the electronic structure of the transition metal sulfideTS2, Phys. Rev. B **83**, 245213 (2011).

[15] B. Radisavljevic, A. Radenovic, J. Brivio, V. Giacometti, and A. Kis, Single-layer MoS2 transistors, Nat. Nanotechnol. **6**, 147 (2011).

[16] K. F. Mak, C. Lee, J. Hone, J. Shan, and T. F. Heinz, Atomically Thin MoS(2): A New Direct-Gap Semiconductor, Phys. Rev. Lett. **105**, 136805 (2010).

[17] W. Zhang, J. Sklenar, B. Hsu, W. J. Jiang, M. B. Jungfleisch, J. Xiao, F. Y. Fradin, Y. H. Liu, J. E. Pearson, J. B. Ketterson, Z. Yang, and A. Hoffmann, Research update: Spin transfer torques in permalloy on monolayer MoS2, Apl Mater. **4**, 032302 (2016).

[18] S. Sinha, S. Pan, S. Choudhury, J. Sinha, and A. Barman, Extrinsic spin–orbit coupling-induced large modulation of gilbert damping coefficient in CoFeB thin film on the graphene stack with different defect density, J. Phys. Chem. C **121**, 17442 (2017).

[19] M. Evelt, H. Ochoa, O. Dzyapko, V. E. Demidov, A. Yurgens, J. Sun, Y. Tserkovnyak, V. Bessonov, A. B. Rinkevich, and S. O. Demokritov, Chiral charge pumping in graphene deposited on a magnetic insulator, Phys. Rev. B **95**, 024408 (2017).

[20] Q. Shao, G. Yu, Y. W. Lan, Y. Shi, M. Y. Li, C. Zheng, X. Zhu, L. J. Li, P. K. Amiri, and K. L. Wang, Strong rashba-edelstein effect-induced spin-orbit torques in monolayer transition metal dichalcogenide/ferromagnet bilayers, Nano Lett. **16**, 7514 (2016).

[21] Z. Y. Zhu, Y. C. Cheng, and U. Schwingenschlogl, Giant spin-orbit-induced spin splitting in two-dimensional transition-metal dichalcogenide semiconductors, Phys. Rev. B **84**, 153402 (2011).

[22] D. MacNeill, G. M. Stiehl, M. H. D. Guimaraes, R. A. Buhrman, J. Park, and D. C. Ralph, Control of spin–orbit torques through crystal symmetry in WTe2/ferromagnet bilayers, Nat. Phys. **13**, 300 (2016).

[23] S. Liang, H. Yang, P. Renucci, B. Tao, P. Laczkowski, S. Mc-Murtry, G. Wang, X. Marie, J. M. George, S. Petit-Watelot, A. Djeffal, S. Mangin, H. Jaffres, and Y. Lu, Electrical spin injection and detection in molybdenum disulfide multilayer channel, Nat. Commun. **8**, 14947 (2017).

[24] B. Li, T. Xing, M. Zhong, L. Huang, N. Lei, J. Zhang, J. Li, and Z. Wei, A two-dimensional Fe-doped SnS2 magnetic semiconductor, Nat. Commun. **8**, 1958 (2017).

[25] C. C. Hsu, Z. Y. Lin, P. C. Chang, H. C. Chiu, H. W. Chen, H. L. Liu, F. Bisio, and W. C. Lin, Magnetic decoupling of Fe coverage across atomic step of MoS2 flakes on SiO2 surface, J. Phys. D: Appl. Phys. **50**, 415001 (2017).

[26] B. Peng *et al.*, Valley polarization of trions and magnetoresistance in heterostructures of MoS2 and yttrium iron garnet, ACS Nano **11**, 12257 (2017).

[27] K.-A. Min, J. Cha, K. Cho, and S. Hong, Ferromagnetic contact between Ni and MoX2(X=S, Se, or Te) with Fermi-level pinning, 2D Mater. **4**, 024006 (2017).

[28] Y. Xu, M. Deb, G. Malinowski, M. Hehn, W. Zhao, and S. Mangin, Ultrafast magnetization manipulation using single femtosecond light and hot-electron pulses, Adv. Mater. **29**, 1703474 (2017).

[29] M. Tang, B. Zhao, W. Zhu, Z. Zhu, Q. Y. Jin, and Z. Zhang, Controllable interfacial coupling effects on the magnetic dynamic properties of perpendicular [Co/Ni]5/Cu/TbCo composite thin films, ACS. Appl. Mater. Interfaces **10**, 5090 (2018).

[30] G. Wu, S. Chen, Y. Ren, Q. Y. Jin, and Z. Zhang, Laser-induced magnetization dynamics in interlayer-coupled [Ni/Co]4/Ru/[Co/Ni]3 perpendicular magnetic films for information storage, ACS Appl. Nano Mater. **2**, 5140 (2019).

[31] K. C. Kuiper, T. Roth, A. J. Schellekens, O. Schmitt, B. Koopmans, M. Cinchetti, and M. Aeschlimann, Spin-orbit enhanced demagnetization rate in Co/Pt-multilayers, Appl. Phys. Lett. **105**, 202402 (2014).

[32] C. Boeglin, E. Beaurepaire, V. Halte, V. Lopez-Flores, C. Stamm, N. Pontius, H. A. Durr, and J. Y. Bigot, Distinguishing the ultrafast dynamics of spin and orbital moments in solids, Nature **465**, 458 (2010).

[33] B. Koopmans, G. Malinowski, F. Dalla Longa, D. Steiauf, M. Fahnle, T. Roth, M. Cinchetti, and M. Aeschlimann, Explaining the paradoxical diversity of ultrafast laser-induced demagnetization, Nat. Mater. **9**, 259 (2010).

[34] P. Deorani and H. Yang, Role of spin mixing conductance in spin pumping: Enhancement of spin pumping efficiency in Ta/Cu/Py structures, Appl. Phys. Lett. **103**, 232408 (2013).

[35] C. T. Boone, H. T. Nembach, J. M. Shaw, and T. J. Silva, Spin transport parameters in metallic multilayers determined by ferromagnetic resonance measurements of spin-pumping, J. Appl. Phys. **113**, 153906 (2013).

[36] H. Lee, L. Wen, M. Pathak, P. Janssen, P. LeClair, C. Alexander, C. K. A. Mewes, and T. Mewes, Spin pumping in Co56Fe24B20multilayer systems, J. Phys. D: Appl. Phys. **41**, 215001 (2008).

[37] J. P. Nibarger, R. Lopusnik, and T. J. Silva, Damping as a function of pulsed field amplitude and bias field in thin film permalloy, Appl. Phys. Lett. **82**, 2112 (2003).

[38] A. Eschenlohr, M. Battiato, P. Maldonado, N. Pontius, T. Kachel, K. Holldack, R. Mitzner, A. Fohlisch, P. M. Oppeneer, and C. Stamm, Ultrafast spin transport as key to femtosecond demagnetization, Nat. Mater. **12**, 332 (2013).

[39] G. Wu, W. Zhu, Z. Zhu, H. Xue, Y. Ren, Y. Liu, Q. Y. Jin, and Z. Zhang, Magnetic precession modes with enhanced frequency and intensity in hard/NM/soft perpendicular magnetic films, Phys. Chem. Chem. Phys. **21**, 16830 (2019).

[40] Z. D. Zhu, B. C. Zhao, W. H. Zhu, M. H. Tang, Y. Ren, Q. Y. Jin, and Z. Z. Zhang, Annealing effect and interlayer modulation on magnetic damping of CoFeB/interlayer/Pt thin films, Appl. Phys. Lett. **113**, 222403 (2018).

[41] S. Husain, A. Kumar, P. Kumar, A. Kumar, V. Barwal, N. Behera, S. Choudhary, P. Svedlindh, and S. Chaudhary, Spin pumping in the Heusler alloy Co2FeAl/MoS2 heterostructure: Ferromagnetic resonance experiment and theory, Phys. Rev. B **98**, 180404 (2018).

[42] A. Capua, S. H. Yang, T. Phung, and S. S. P. Parkin, Determination of intrinsic damping of perpendicularly magnetized ultrathin films from time-resolved precessional magnetization measurements, Phys. Rev. B **92**, 224402 (2015).

[43] Y. Sun, H. Chang, M. Kabatek, Y. Y. Song, Z. Wang, M. Jantz, W. Schneider, M. Wu, E. Montoya, B. Kardasz, B. Heinrich, S. G. te Velthuis, H. Schultheiss, and A. Hoffmann, Damping in Yttrium Iron Garnet Nanoscale Films Capped by Platinum, Phys. Rev. Lett. **111**, 106601 (2013).

[44] Y. Tserkovnyak, A. Brataas, and G. E. W. Bauer, Spin pumping and magnetization dynamics in metallic multilayers, Phys. Rev. B **66**, 224403 (2002).

[45] J. M. Shaw, H. T. Nembach, and T. J. Silva, Determination of spin pumping as a source of linewidth in sputtered

Co90Fe10/Pd multilayers by use of broadband ferromagnetic resonance spectroscopy, Phys. Rev. B **85**, 054412 (2012).

[46] Y. Li, F. Zeng, S. S. Zhang, H. Shin, H. Saglam, V. Karakas, O. Ozatay, J. E. Pearson, O. G. Heinonen, Y. Wu, A. Hoffmann, and W. Zhang, Giant Anisotropy of Gilbert Damping in Epitaxial CoFe Films, Phys. Rev. Lett. **122**, 117203 (2019).

[47] L. Chen, S. Mankovsky, S. Wimmer, M. A. W. Schoen, H. S. Körner, M. Kronseder, D. Schuh, D. Bougeard, H. Ebert, D. Weiss, and C. H. Back, Emergence of anisotropic Gilbert damping in ultrathin Fe layers on GaAs(001), Nat. Phys. **14**, 490 (2018).

[48] H. Jiao and G. E. Bauer, Spin Backflow and ac Voltage Generation by Spin Pumping and the Inverse Spin Hall Effect, Phys. Rev. Lett. **110**, 217602 (2013).

[49] D. Jhajhria, N. Behera, D. K. Pandya, and S. Chaudhary, Dependence of spin pumping in W/CoFeB heterostructures on the structural phase of tungsten, Phys. Rev. B **99**, 014430 (2019).